The circumstellar envelopes around three protostars in Taurus

Claire J. Chandler
Mullard Radio Astronomy Observatory, Cavendish Laboratory, Madingley Road, Cambridge CB3 0HE

Mary Barsony
Physics Department, University of California, Riverside, CA 92521, USA

and

Toby J. T. Moore
Astrophysics Research Institute, Liverpool John Moores University, Byrom Street, Liverpool L3 3AF

ABSTRACT

We have investigated the distribution of circumstellar material around three Class I protostars in Taurus. TMC1 (IRAS 04381+2540), TMC1A (IRAS 04365+2535), and Haro 6-10 (IRAS 04263+2426) have all been mapped in 790-μm dust continuum emission using the James Clerk Maxwell Telescope, and TMC1A has also been imaged at λ 1.1 mm. In addition, we present a ^{12}CO J=2–1 map of Haro 6-10 obtained using the Caltech Submillimeter Observatory. The dust emission from TMC1 is extended and is oriented perpendicular to its outflow, with little evidence for a compact disc component. The submillimetre emission from TMC1A is centrally peaked, with a weak extension in the direction of the outflow at both 790 μm and 1.1 mm. It is possible that the interaction of the outflow with the surrounding cloud is heating the dust. The emission from Haro 6-10 is oriented roughly perpendicular to the direction of several HH objects in the region. There is no clear bipolar molecular outflow structure in the CO(2–1) map, and the relatively low velocities observed in the line wings suggest that any such system must lie close to the plane of the sky.

If the dust emission from the envelopes is optically thin and a temperature distribution can be specified, the broadband spectral energy distribution (SED) can be used to constrain the density profile. We isolate the envelope SEDs for our sources by subtracting possible disc and wind components from the submillimetre flux densities, and use a simple model to derive the radial power-law dependence of the density in each case. We find that for a density distribution $\rho \propto r^{-p}$ the values of p are 0.93 ± 0.25, 0.81 ± 0.30, and 1.22 ± 0.11 for TMC1, TMC1A and Haro 6-10 respectively, which for all but Haro 6-10 is considerably shallower than can currently

be explained by collapse theory. We suggest that the envelopes around TMC1 and TMC1A may be rotationally supported, but that the Haro 6-10 envelope may still be infalling. The envelope masses are $\sim$ 0.02–0.03 $M_\odot$ in all cases.

Subject headings: Stars: formation — circumstellar matter — dust, extinction — ISM: structure — ISM: individual (TMC1, TMC1A, Haro 6-10)

1. Introduction

The distribution of the circumstellar material around young protostars potentially provides considerable information concerning the history of their evolution. Models for the collapse of a dense core in a molecular cloud and its subsequent evolution to form an embedded protostar make predictions about the density structure, which is a function of both radius and time. In the picture advocated by Shu (1977) and Shu, Adams, & Lizano (1987), material in an isothermal cloud core approaches the structure of a singular isothermal sphere with $\rho \propto r^{-2}$ quasi-statically, perhaps mediated by ambipolar diffusion (Lizano & Shu 1989). Such a configuration is highly unstable, and a perturbation may initiate free-fall collapse onto a hydrostatic core at the centre, resulting in an infall region where $\rho \propto r^{-1.5}$, expanding outwards at the local sound speed. This model characteristically predicts a constant mass accretion rate onto the hydrostatic core from the surrounding cloud.

Recent numerical hydrodynamic calculations of the collapse such as those carried out by Foster & Chevalier (1993) suggest that the evolution to a $\rho \propto r^{-2}$ structure may not necessarily be quasi-static, but may be initiated by perturbations in the cloud core while the central regions are still relatively uniform in density. In this case the central flat part of the core collapses rather quickly giving a high initial accretion rate, and in the outer regions the gas is already infalling at approximately three times the sound speed when the $\rho \propto r^{-2}$ density distribution is established. Nevertheless, if the cloud is large enough, it may pass through a phase of constant accretion as in the singular isothermal sphere model. A flattened density profile in the inner regions at early times may arise naturally from the formation of cloud cores via ambipolar diffusion (e.g., Ciolek & Mouschovias 1994).

The pre-stellar cores mapped in millimetre and submillimetre dust continuum emission by Ward-Thompson et al. (1994) and André, Ward-Thompson, & Motte (1996) typically show somewhat flattened density profiles ($\rho \propto r^{-1.2}$) within radii of $\sim$ 4000 AU. For deeply embedded (Class 0) protostars where the density profiles in the surrounding envelope have been measured, a few show the $\rho \propto r^{-1.5}$ consistent with free-fall collapse (e.g., L1527: Ladd et al. 1991; B335:

Chandler & Sargent 1993); others, however, have envelopes with surprisingly shallow density distributions of $\rho \propto r^{-0.5}$ (e.g., VLA1623: André, Ward-Thompson, & Barsony 1993). In order to investigate the distribution of circumstellar material around slightly older, Class I protostars, for comparison with the more deeply embedded objects and the pre-stellar cores, we have carried out observations of the submillimetre dust emission from TMC1A (IRAS 04365+2535), TMC1 (IRAS 04381+2540), and Haro 6-10 (IRAS 04263+2426, also known as GV Tau B), in Taurus ($D = 140$ pc: Elias 1978; Kenyon, Dobrzycka, & Hartmann 1994b). We have also obtained a map of the ^{12}CO J=2–1 emission from a 2×2 arcmin^2 area centred on Haro 6-10, to study structure in the high-velocity molecular emission and its relationship to the dust envelope. Since near-infrared emission is detected from all these protostars (either photospheric in origin, or reflection nebulosity close to the star) most of the far-infrared and submillimetre dust emission from their circumstellar envelopes can be assumed to be optically thin. We use this information to demonstrate how spectral energy distributions (SEDs) of optically thin envelopes can constrain density profiles from a simple model.

2. Observations

2.1. Dust continuum

The submillimetre and millimetre observations were made using the ^{3}He-cooled bolometer UKT14 (Duncan et al. 1990) on the 15-m James Clerk Maxwell Telescope (JCMT) on Mauna Kea, Hawaii, in 1990 September and 1991 September. During the 1990 observing run maps of TMC1A were obtained at wavelengths of 1.1 mm and 790 μm, using chop throws of 60 and 120 arcsec in azimuth. The beam sizes were approximately 19 and 13.5 arcsec at 1.1 mm and 790 μm respectively, and the mapping was carried out in a point-by-point photometry mode with points spaced at 8 and 6 arcsec to give fully-sampled maps at both wavelengths. Mars was used as the primary flux density calibrator. The sky was stable but had fairly high zenith opacities of 0.15 at 1.1 mm, and 0.9 at 790 μm.

During the second observing run, in 1991, the weather was considerably better and photometry of all our program sources was obtained at wavelengths of 2 mm, 1.3 mm, 1.1 mm, 790 μm, and 450 μm, using chop throws of 60 and 120 arcsec in azimuth. Multiple apertures were used at 790 μm to provide both the diffraction-limited resolution of 13.5 arcsec for mapping, and a larger half-power beam width of 16 arcsec for photometry. At 450 μm the largest aperture gave a beam width of 19 arcsec; at the other wavelengths the resolution was diffraction-limited. Point-by-point maps were made at 790 μm of TMC1 and Haro 6-10. Jupiter and Mars were used as primary flux density calibrators, and W3(OH) and CRL618 were adopted as secondary calibrators [see Barsony & Chandler (1993) for their derived flux densities]. For most of the 1991 observations the zenith

opacity at λ 1.3 mm, monitored using the radiometer at the Caltech Submillimeter Observatory (CSO), was in the range 0.05 to 0.1. The observations are summarized in Table 1. The uncertainty in the absolute flux density scale at each wavelength is given in the notes to Table 2.

We have also used the IRAS high resolution processing facility 'HIRES' to obtain new images of all our program sources in the IRAS 12, 25, 60 and 100 μm bands (Aumann, Fowler, & Melnyk 1990). None of the sources was resolved in these new images, although the mean far-infrared positions in the HIRES-processed data are within 4 arcsec of the positions listed in Table 1, a considerable improvement over those in the IRAS Point Source Catalog (PSC). We have used these new images to obtain colour-corrected far-infrared flux densities for our sources, which are given in Table 2. The errors quoted include the statistical uncertainty from the PSC, and calibration uncertainties of 5, 7, 7 and 10 per cent at 12, 25, 60 and 100 μm respectively (Neugebauer et al. 1988).

2.2. CO(2–1) mapping of Haro 6-10

The ^{12}CO J=2–1 observations of Haro 6-10 were carried out at the CSO 10.4-m telescope on Mauna Kea, Hawaii, in 1991 December. The spectra were obtained using the facility 230 GHz receiver, and an acousto-optical spectrometer with a channel spacing of 49 kHz (63 m s^{-1}) and a total bandwidth of 50 MHz (65 km s^{-1}). The beam width at 230 GHz is approximately 31 arcsec, and the pointing was updated every 2 hours during the observations. The measurements were made using position switching, initially with an off-position at $(\Delta\alpha, \Delta\delta) = (-2^\circ, 0^\circ)$. Emission was later found at this off-position, so a deep spectrum was obtained at this location using a reference position relative to Haro 6-10 of $(-5^\circ, -1^\circ)$, and was added to the Haro 6-10 spectra during the data reduction. Spectra were obtained corrected for atmospheric absorption (in units of T_A^*), and have had a linear baseline removed. They have then been converted to main-beam brightness temperature, $T_{\rm MB}$, by dividing by the main-beam efficiency, $\eta_{\rm MB}$. Measurements of Jupiter obtained on the same night as the Haro 6-10 observations gave $\eta_{\rm MB}$ = 0.73 (see also Mangum 1993). An area of 2×2 arcmin^2 centred on Haro 6-10 was mapped with a point spacing of 15 arcsec.

3. Results

3.1. Images

3.1.1. Submillimetre dust continuum

Our submillimetre continuum maps of Haro 6-10, TMC1, and TMC1A, are displayed in Fig. 1. Haro 6-10 is a 1.2-arcsec binary system oriented north-south (Leinert & Haas 1989). A Gaussian fit to our 790 μm map gives a FWHM of $\sim 30 \times 22$ arcsec^2 at PA $\sim 135^\circ$, indicating that the emission is extended relative to the 13.5-arcsec beam. However, it is also clear that a Gaussian distribution is not a particularly good model for the data. The Herbig-Haro objects thought to be excited by Haro 6-10 are oriented at PA $\sim 65^\circ$ (Strom et al. 1986), and early measurements of CO(1–0) emission from several positions suggested there may be a molecular outflow oriented roughly east-west (Edwards & Snell 1984). High velocity CO emission is also reported in the interferometric snap-shot survey for compact outflows by Terebey, Vogel, & Myers (1989). The Haro 6-10 outflow is discussed further below.

TMC1 and TMC1A are among the cooler Class I protostars in the Taurus cloud, as defined by their bolometric temperature (Chen et al. 1995). They both lie in the Taurus Molecular Ring. In 790 μm emission TMC1 displays considerable extended structure, and the main peak in the map is elongated with a position angle of approximately 75°. The outflow from this source is oriented north-south (Chandler et al. 1996), so the submillimetre emission may be tracing mainly the location of remnant circumstellar material, left over after the outflow has evacuated its cavity. A similar structure is observed in HCO^+ emission by Hogerheijde et al. (1997). The outflow from TMC1A is at a position angle of approximately -10° (Chandler et al. 1996), so in this source the 790 μm and 1.1 mm dust emission appears to be more or less aligned with the outflow direction. The near-infrared nebulosity associated with the outflow is particularly bright towards the blueshifted outflow lobe in the north, which is also the stronger of the two lobes in CO(2–1) emission; its coincidence with thermal dust emission suggests that some of the near-infrared emission could be due to heated dust in the flow. However, comparison with the HCO^+(1–0) map presented by Hogerheijde et al. (1997) illustrates that dense gas lies directly to the north of the infrared source, so the mm/submm dust emission may also be tracing a region of enhanced column density. The dust emission is unresolved east-west at both wavelengths in TMC1A.

3.1.2. CO(2–1) emission from Haro 6-10

In Fig. 2 we present a spectrum of the CO(2–1) emission from Haro 6-10 averaged over the entire 2×2 arcmin^2 mapped, and also a spectrum centred on the embedded protostar. A

comparison of our averaged CO(2–1) line with the CO(1–0) spectrum presented by Edwards & Snell (1984), obtained using a 45-arcsec beam, shows extremely good agreement in the details of the observed velocity structure. The systemic LSR velocity of Haro 6-10, as measured by the more optically thin tracers ^{13}CO(1–0) and C^{18}O(1–0), is 6.5 km s^{-1} (Edwards & Snell 1984; Terebey et al. 1989). Many of the ^{12}CO(2–1) spectra also show the optically-thin, blueshifted component at $V_{\rm LSR} = 4$ km s^{-1}, first detected by Edwards & Snell.

Fig. 3 shows the blue- and redshifted emission in the line wings, integrated from $|V - V_{\rm LSR}| = 3$ to 6 km s^{-1}, chosen to avoid contamination from the 4 km s^{-1} component. The structure of the CO(2–1) emission is in good agreements with the CO(3–2) map presented by Hogerheijde et al. (1998), and in neither image is there clear bipolar structure aligned with the HH objects. However, the relatively low velocities observed in the line wings suggest the outflow may be close to the plane of the sky, in which case overlapping red- and blueshifted emission might be expected and may not be as spatially separate as is observed for TMC1 and TMC1A (Chandler et al. 1996). A high inclination for the outflow axis to the line of sight is also indicated by the low velocities observed in the HH objects (Cohen & Fuller 1985), which are blueshifted with respect to the cloud by approximately -32 km s^{-1} (Strom et al. 1986). Assuming a space velocity of 200 km s^{-1} typically observed for low-inclination HH objects and protostellar jets, the velocity observed for the Haro 6-10 HH objects implies that the flow lies at an inclination $i \gtrsim 80^\circ$. It is therefore not surprising that the high-velocity CO(2–1) emission is structurally complex, especially as much of the surrounding molecular cloud has probably already been severely disrupted by the outflow: the dense gas traced by HCO$^+$(1–0) emission is located primarily towards the north-east of the embedded protostellar system (Hogerheijde et al. 1997), while the cloud in the direction of the HH objects seems already to have been dispersed. Furthermore, the binary nature of Haro 6-10 may mean that at some stage in the past multiple outflows have left their mark on the kinematics of the molecular gas.

We note that Hogerheijde et al. (1998) conclude, from the lack of clear bipolar structure and the "broad line wings," that $i < 45^\circ$. However, from their position-velocity diagrams the velocity extent of the outflow from Haro 6-10 is smaller than either TMC1 or TMC1A, for which i lies in the range 40 to 70° (Chandler et al. 1996), and is more comparable to that observed for other sources in their sample whose outflows lie close to the plane of the sky. It is clear that the question of the inclination of the Haro 6-10 outflow remains open.

3.2. Spectral energy distributions

The results of the millimetre and submillimetre photometry are listed in Table 2, and plotted together with other measurements from the literature as SEDs in Fig. 4. They are displayed in

order of increasing bolometric temperature, $T_{\rm bol}$, which are given by Chen et al. (1995) as 139 K, 172 K, and 409 K for TMC1, TMC1A, and Haro 6-10 respectively. This trend is clearly evident in Fig. 4. For the large sample of sources used by Chen et al. in their study, $T_{\rm bol}$ was found to increase monotonically from embedded Class 0/I sources, to classical T Tauri stars, to weak-line T Tauri stars. Within each subgroup, e.g., Class 0/I protostars, a correlation was also found between $T_{\rm bol}$ and protostellar age derived from a model based on the collapse of an isothermal sphere (Shu 1977; Terebey, Shu, & Cassen 1984, hereafter TSC; Kenyon, Calvet, & Hartmann 1993, hereafter KCH). If this is the case, we would interpret the trend in $T_{\rm bol}$ illustrated in Fig. 4 as an increase in age, and using the $T_{\rm bol}$–age relationship derived by Chen et al. would obtain ages ranging from $\sim 2 \times 10^4$ yr (TMC1 and TMC1A) to $\sim 1 \times 10^5$ yr (Haro 6-10).

4. Discussion

The optical through far-infrared emission from all three protostars has been modelled by KCH, who base their analysis on the collapsing, rotating isothermal sphere of TSC. Their model has a $\rho \propto r^{-1.5}$ density distribution throughout the envelope, flattening to a disc inside the centrifugal radius. The outer radius for the envelope is 3000 AU, or $\sim$ 20 arcsec at the distance of the Taurus molecular cloud. Given the size of our maps we might therefore expect our submillimetre flux densities to be lower than predicted by these models. We do, however, find very good agreement between the long-wavelength emission predicted by the KCH models and our measurements of Haro 6-10. For TMC1 and TMC1A the models under-predict the submillimetre flux density, by approximately 50 per cent and a factor of 3 respectively. It is possible that the technique used by KCH to calculate the radiative equilibrium temperature may contribute to this effect. They assume spherical symmetry in deriving the temperature, and use the flattened distribution from TSC only in calculating the emergent flux. If an asymmetrical distribution were used, perhaps including outflow cavities in the envelope, then radiation from the central star and disc could travel unattenuated to large radii along the poles of the system, and the angle-averaged temperature distribution would be flatter than was found by KCH. However, it is doubtful that this could account fully for the discrepancy observed for TMC1A. An alternative explanation, in which we explore the possibility that the density distribution is flatter than $\rho \propto r^{-1.5}$, is described below.

4.1. Disc and envelope emission

At far-infrared through to millimetre wavelengths the contributions to the emission from circumstellar discs and envelopes must be separated before either component can be analysed.

The spectral index of the disc emission is expected to be flatter than for the envelope because of high optical depths in the disc, and because the frequency dependence of the dust opacity, β, defined by $\kappa_\nu \propto \nu^\beta$, may be lower in discs compared with molecular clouds (Beckwith et al. 1990; Mannings & Emerson 1994; Chandler et al. 1995). The disc emission may therefore be important at $\lambda \gtrsim 1$ mm, an effect clearly visible in the KCH models. For wavelengths $\lambda \lesssim 1$ mm, however, Terebey, Chandler, & André (1993) argue that single-dish measurements of embedded protostars are dominated by emission from the envelope. If a separate disc component with a power-law dependence on frequency is present, it should manifest itself as a break in the spectral slope at long wavelengths.

No spectral break corresponding to separate disc and envelope components is observed for TMC1, and the 2.7 mm interferometer flux is also observed to be a function of beam size [see Fig. 4, which plots the flux reported by Hogerheijde et al. (1997) in a 3-arcsec beam as a filled circle, and the flux in a 9-arcsec beam from Brown & Chandler (1998) as an open circle], suggesting the emission is extended. The signal-to-noise ratio of both datasets is rather low, but the emission is not particularly point-like. Evidence for the presence of a disc in TMC1 is therefore inconclusive, and we include all the long-wavelength points shown as open circles in Fig. 4 in our analysis of the envelope emission.

The interferometer fluxes of TMC1A do show evidence for emission at $\lambda \approx 3$ mm in excess of the envelope component detected at $\lambda \lesssim 1$ mm. Assuming a long-wavelength disc spectrum $F_\nu \propto \nu^\alpha$ where $\alpha \gtrsim 2$, the 2.7 mm flux density reported by Hogerheijde et al. (1997) implies that at least 50, 40 and 25 per cent of the total emission at 1.3 mm, 1.1 mm and 790 μm respectively may originate in the disc. The strongly centrally-peaked maps of TMC1A in Fig. 1 also support this picture. Using the $\lambda = 2.7$ mm and 3.4 mm measurements of Hogerheijde et al., and assuming that the absolute calibration uncertainty at each wavelength was 10 per cent, the spectral index of the compact dust component is $\alpha = 2.6 \pm 0.8$. Although the small frequency range of the measurements make α very uncertain, a value of 2.6 is not too different from that commonly measured for T Tauri stars or protostellar discs (e.g., Lay et al. 1994; Koerner, Chandler, & Sargent 1995; Chandler et al. 1995). We have therefore used $\alpha = 2.6$ to separate the disc and envelope contributions to the flux densities listed in Table 2.

A point-like millimetre source associated with Haro 6-10 has been detected by Hogerheijde et al. (1997). Its spectral index is $\alpha = -0.2 \pm 1.0$, casting doubt on whether this emission originates from dust. Indeed, an unresolved 5 GHz source was found within 1 arcsec of the infrared position by Bieging, Cohen, & Schwartz (1984), and the flux densities detected at $\lambda \approx 3$ mm are consistent with arising in an ionized wind from the embedded protostar, with $\alpha \approx 0.8$. The contribution from this wind to the submillimetre emission is at most 25 per cent (at 1.3 mm), but we have, nevertheless, subtracted this component from the flux densities used in our envelope analysis. We

note that the interpretation of the compact millimetre source as an ionized wind rather than a disc is in contradiction to the results of Hogerheijde et al., who did not consider the possibility of free-free emission. Instead, they assumed the emission to originate in a disc, and after extrapolating to higher frequencies using a typical disc spectrum, suggested that all the 1.1 mm emission detected by Moriarty-Schieven et al. (1994) could be explained by a disc. However, the success of the modelling carried out by KCH in which a much smaller disc was used to fit the short-wavelength data for Haro 6-10 than was needed for either TMC1 or TMC1A, leads us to allocate all the submillimetre emission from Haro 6-10 to either the ionized wind or the dust envelope.

4.2. A model for far-IR/mm dust emission from optically-thin envelopes

The shape of the envelope SED at far-infrared through to millimetre wavelengths is defined by the relative amounts of material at different temperatures included in the measurements. The method of inverting an optically-thin dust SED using maximum entropy techniques to derive the mass per unit temperature interval illustrates this principle (Hobson & Padman 1994), and also shows that the amount of cold dust, in particular, may not be well constrained by the data. However, if extra conditions are applied to the temperature and density distributions of the material, for example, that they are power-law functions of radius, then the SED may be used to derive those distributions. We have therefore constructed a model which uses χ^2-minimization to fit for the density power-law, to examine whether alternative density distributions are more successful at reproducing the submillimetre fluxes of Haro 6-10, TMC1, and TMC1A, than the $\rho \propto r^{-1.5}$ assumed by KCH. Our model is similar to that described by André & Montmerle (1994), who use an optically-thin envelope with power-law temperature and density distributions to derive mass-weighted mean temperatures and envelope masses for Class I protostars in the ρ Ophiuchi cloud. However, because they typically had only the IRAS fluxes and a single 1.3 mm measurement, they performed a small search of parameter space for just one source, and used the value derived for that source, $\rho \propto r^{-0.5}$, for the rest of their sample. With the submillimetre points to fill in the SEDs of our Taurus protostars, we are able to compare the envelope distributions of different objects.

We fit only the data at $\lambda \gtrsim 20$ μm, and therefore use a single power law for the dust opacity throughout the far-infrared and submillimetre, $\kappa_\nu = 0.01(\nu/10^{12}\ \mathrm{Hz})^\beta\ \mathrm{kg\ m^{-2}}$ (cf. Beckwith & Sargent 1991). The temperature distribution in the model is a radial power law, $T \propto r^{-q}$, where $q = 2/(4+\beta)$, as long as $T \geq 10$ K. At larger radii a constant $T = 10$ K is assumed. The density profile is $\rho \propto r^{-p}$ between the inner radius of the envelope, r_0, and the outer radius, $R_{\max}$, which is taken to be 2500 AU (≈ 18 arcsec for Taurus), comparable to the area covered by our maps. In

the optically-thin limit, the flux density emitted by the envelope is therefore

$$F_\nu = \frac{4\pi\kappa_\nu}{D^2}\int_{r_0}^{R_{\rm max}} \rho(r) B_\nu[T(r)] r^2 dr.$$

We then vary the envelope mass, $M_{\rm env}$, r_0, the temperature at a fiducial radius, T_0, p, and β (which also defines q) to fit the SED. It is clear that at least 6 data points are therefore needed to constrain the model. We discard those fits for which the peak optical depth through the envelope to the source is greater than unity at $\lambda \gtrsim 20$ μm, to maintain agreement with the detection of near-infrared emission very close to the embedded protostar in all three cases, and to keep the model self-consistent.

We also ensure that the normalization of the temperature distribution, T_0, is consistent with more detailed radiative transfer calculations. Although our model for the temperature distribution in the envelope as a power law is very simple, the value of q predicted, in the range 0.3 to 0.4 for β = 1 to 2, agrees well with radiative transfer modelling (e.g., Scoville & Kwan 1976; Butner et al. 1990; Wolfire & Churchwell 1994; Preibisch, Sonnhalter, & Yorke 1995). The analytic expressions derived by Scoville & Kwan (1976) for the scaling of $T(r)$ with radius and central source luminosity, $L_{\rm bol}$, can be generalized to

$$T(r) \approx 50\, Q_{\rm abs}^{-q/2} \left(\frac{r}{2\times10^{15}\ {\rm m}}\right)^{-q} \left(\frac{L_{\rm bol}}{10^5\ {\rm L}_\odot}\right)^{q/2} \quad {\rm K}, \qquad (1)$$

where $Q_{\rm abs}$ is the absorption efficiency of a dust grain at $\lambda = 50$ μm and $q = 2/(4+\beta)$. Since $Q_{\rm abs} \leq 1$, this expression provides a lower limit to $T(r)$. The numerical coefficient $50\, Q_{\rm abs}^{-q/2}$ may then be compared with the output from radiative transfer codes. The modelling presented by Butner et al. (1990) agrees with Equation 1 only if $Q_{\rm abs} = 1$, while the results from Wolfire & Churchwell (1994) and Preibisch et al. (1995) correspond to $Q_{\rm abs}^{-q/2} \sim 1.2$–$1.6$. Fits to our data with solutions for T_0 which would need $Q_{\rm abs} > 1$ are therefore also discounted, although these are generally also the solutions which do not comply with the requirement that the emission be optically thin for all $\lambda \gtrsim 20$ μm.

The value of q does not change much for plausible values of β, so the effect of varying β on the model SED is primarily felt through the dust opacity. Steep density gradients, where p is large, have relatively large amounts of warm dust and the ratio of far-infrared to submillimetre flux is high, resulting in narrow SEDs. Flat density gradients produce broad spectra. In general, the long-wavelength data define β; the ratio of the far-infrared to submillimetre flux and the shape of the far-infrared spectrum constrain p; the absolute normalization gives $M_{\rm env}$; T_0 comes mainly from the low-frequency far-infrared turnover, and r_0 (or equivalently, the maximum temperature of material included in the fits) is determined by the high-frequency turnover. The best-fit envelope models derived using the Levenberg-Marquardt method (Press et al. 1986) are plotted along with

the fluxes we attribute to the envelope in Fig. 5, and are summarized in Table 3. As the far-infrared photometry measurements of Haro 6-10 from Cohen et al. (1984) are consistently lower than the IRAS points (Fig. 4), we did not use the 20 μm point in the fit for this source. Instead, we included the 12 μm IRAS flux to constrain the short wavelength emission in the model.

The errors on the fitted parameters obtained from the covariance matrix are also given in Table 3. They illustrate the range of values that provide acceptable fits to the data, given the formulation of the model. They show that the fits are relatively insensitive to the value of r_0, which is because there is no real constraint on the high-frequency turnover unless the high-frequency emission from the envelope can be separated from other emission components by some other method. The inclusion of the 12 μm point in the fit for Haro 6-10 is reflected directly in a smaller value of r_0 for that source. The dependence of $M_{\rm env}$ on β is shown in the large range of both values which provide acceptable fits, especially for TMC1A, with high values of β corresponding to high values of $M_{\rm env}$. On the other hand, the radial power-law of the density dependence, p, is relatively well-constrained by our model. For the protostars TMC1 and TMC1A the density gradients we derive are consistently flatter than either the $\rho \propto r^{-2}$ or $r^{-1.5}$ of the TSC collapse model. Only for Haro 6-10, which from its dust spectrum would be interpreted as being older than the other two sources, is the density distribution close to these theoretical predictions. Similarly flat density distributions have also been derived from the SEDs of IRAS 04016+2610 (Myers et al. 1987) and EL29 (André & Montmerle 1994). In column 6 of Table 3 we give the range of values for the temperature at a radius of 100 AU, T_{100}, which would be consistent with the radiative transfer modelling of Butner et al. (1990), Wolfire & Churchwell (1994), and Preibisch et al. (1995). Our model results are clearly in good agreement with the predictions of these more detailed codes. The mass-weighted mean temperatures of the envelopes in the best-fit models, $\langle T \rangle$, increase with source luminosity, and are similar to those derived for Class I protostars in ρ Oph by André & Montmerle (1994).

Since the submillimetre emission from TMC1A is aligned with the outflow, some fraction of the dust in the envelope may be heated by shocks where the wind interacts with the surrounding molecular gas, rather than by radiative heating from the central star and disc. In order to assess the effect of heating by the outflow on the density distribution derived from the SED, we need to remember that the SED models are actually merely fitting for the mass as a function of temperature. By assuming that the same radial temperature and density distributions apply in all directions except the outflow cavity, and by specifying the temperature power law, we are then able to invert the SED to obtain the density distribution. If some of the dust in the outflow cavity is warmer than would be predicted by this model, it can be considered as contributing a separate emission component which needs to be taken into account before fitting the envelope. The outflow-heated dust is a warm component which, in the model, is assumed to reside at small radii. Thus if this warm component were removed, the effect would be to make the density distributions even

more flat than those derived without taking the outflow into account. If, however, the extended submillimetre emission from TMC1A is caused by a volume and column density enhancement in the molecular cloud toward the blue outflow lobe, as discussed earlier, then it will have the opposite effect, producing an artifically flat density distribution.

The flattened dust distributions observed for TMC1 and Haro 6-10, on the other hand, are approximately perpendicular to their respective outflows. It therefore seems unlikely that the heating of dust by the outflows is a major contributor to the observed morphologies, and as long as the envelope remains optically thin to both the heating radiation from the central source and the emission from the dust, the temperature distribution given by equation (1) will apply. The density distribution derived from the model will then be an average over all directions except the outflow cavity. If in some directions the density distribution falls off more steeply than is given by the value of p in Table 3, then towards others it will be less steep.

The shallow density profiles which have now been observed for several protostars are difficult to explain if the dominant motion in the circumstellar material is infall. Although pre-stellar cores may have flat density distributions in their inner regions (e.g., Ward-Thompson et al. 1994), *all* the hydrodynamical models, most of which do start from uniform density distributions, quickly establish $\rho \propto r^{-2}$ when the central protostar forms and then experience a phase of $\rho \propto r^{-1.5}$ later on during the collapse (e.g., Foster & Chevalier 1993). It is therefore difficult to avoid passing through a regime with $p \sim 1.5$ to 2 during dynamical collapse. However, all the sources studied here have a relatively small fraction of the total mass in the envelope, suggesting that the bulk of the stellar mass has already been accumulated. The remaining circumstellar gas is presumably the material with the highest initial specific angular momentum in the cloud, and could therefore be supported against collapse by rotation. Indeed, the modelling of the gas dynamics of TMC1 and TMC1A by Brown & Chandler (1998) suggest that rotation can explain kinematic features in the ^{13}CO and C^{18}O J=1–0 emission, with no need for an infall component (see also Ohashi et al. 1997). While this explanation may be adequate for the older Class I protostars, it clearly cannot hold for Class 0 sources such as VLA1623 (André et al. 1993), if Class 0 objects are still in the process of building up their stellar masses via infall and accretion. Theories of collapse and early protostellar evolution have yet to account for low values of p. Haro 6-10, on the other hand, displays active signs of ongoing accretion (Herbst, Koresko, & Leinert 1995), more consistent with its density distribution being similar to that predicted for free-fall collapse. This hypothesis could clearly be tested using high-resolution interferometric observations of the kinematics of the circumstellar gas.

5. Conclusions

The circumstellar envelopes of Class I protostars are optically thin to far-infrared and millimetre dust emission. This simplification of the radiative transfer has enabled us to undertake an investigation of the density distribution of envelope material for three sources in Taurus: TMC1, TMC1A, and Haro 6-10. We have combined submillimetre imaging and photometry, and new IRAS fluxes from HIRES-processed data, with previously published photometry to produce complete spectral energy distributions. Maps of all three sources have been obtained at λ = 790 μm, and TMC1A has also been mapped at 1.1 mm. To enable a comparison between the spatial distribution of the circumstellar gas and the direction of the outflow from each source we have also obtained a map of the CO(2–1) emission from Haro 6-10 at 31-arcsec resolution; similar images of TMC1 and TMC1A have already been published (Chandler et al. 1996).

The 790 μm dust emission from TMC1 is extended perpendicular to the direction of its outflow, and a comparison of the emission with mm interferometer data provides little evidence for a compact disc component. The millimetre and submillimetre emission from TMC1A, however, is centrally peaked at the position of the infrared source. There also appears to be an extension along the outflow direction at both 790 μm and 1.1 mm. It is possible that the interaction of the outflow with the surrounding cloud is heating the dust. The emission from Haro 6-10 is oriented roughly perpendicular to the position angle of several HH objects thought to be driven by the embedded protostellar binary system. Wings in the CO(2–1) spectra of Haro 6-10 extend approximately 6 km s^{-1} beyond the systemic LSR velocity, suggesting that any high-velocity outflow from this source must lie with its symmetry axis close to the plane of the sky. This orientation is also inferred from the low velocities of the HH objects measured by Cohen & Fuller (1985). There is no clear bipolar structure in the 2×2 arcmin^2 area mapped in CO(2–1) emission, possibly due to a combination of the inclination and relatively old age of the source.

The shape of optically-thin dust SEDs are determined directly by the amounts of dust at different temperatures included in the measurements. If the SED can be inverted to find the mass per unit temperature interval, and the temperature distribution is specified, then the SED can be used to derive the density distribution. We have separated the envelope SEDs for our three protostars by subtracting contributions to the long-wavelength fluxes from possible disc and wind components, and have used a simple model and χ^2-minimisation to derive the power-law radial dependence of the density, p, where $\rho \propto r^{-p}$. We assume the temperature distribution is also a radial power law, $T \propto r^{-q}$, where $q = 2/(4+\beta)$ and β is the frequency dependence of the dust opacity, and fit for the envelope mass, the temperature normalization, β, p, and the inner radius, r_0. We also ensure that the temperature distribution is consistent with more detailed radiative transfer codes in the literature. The solutions are relatively insensitive to r_0, and because the value of q is almost constant for β in the range 1 to 2, the value of p helps to specify the overall shape of the

far-infrared through to millimetre emission, and so is well-constrained by the model.

We find values for p of 0.93 ± 0.25, 0.81 ± 0.30, and 1.22 ± 0.11 for TMC1, TMC1A and Haro 6-10 respectively, which for all but Haro 6-10 is considerably shallower than the $\rho \propto r^{-2}$ or $r^{-1.5}$ predicted for hydrostatically supported or freely-infalling cloud cores. There is some evidence that the the envelopes around TMC1 and TMC1A may be rotationally supported, but the Haro 6-10 envelope may still be undergoing collapse. The envelope masses are ~ 0.02–0.03 $M_\odot$ for all three sources, which is probably less than 10 per cent of the central stellar mass. Deep imaging of the extended dust emission using the new submillimetre cameras such as SCUBA on the JCMT and SHARC on the CSO will undoubtedly be extremely important for providing improved constraints on circumstellar density distributions.

Acknowledgments

We thank the referee, Derek Ward-Thompson, for pointing out some areas of the original text which needed clarification. CJC was supported by an Advanced Fellowship from the Particle Physics and Astronomy Research Council during most of this work, and MB acknowledges the receipt of a National Science Foundation CAREER Award. The James Clerk Maxwell Telescope is operated by the Joint Astronomy Centre on behalf of the Particle Physics and Astronomy Research Council of the United Kingdom, the Netherlands Organisation for Scientific Research, and the National Research Council of Canada. The Caltech Submillimeter Observatory is supported by the National Science Foundation, contract AST 96-15025.

REFERENCES

André, P., Montmerle, T., 1994, ApJ, 420, 837

André, P., Ward-Thompson, D., Barsony, M., 1993, ApJ, 406, 122

André, P., Ward-Thompson, D., Motte, F., 1996, A&A, 314, 625

Aumann, H. H., Fowler, J. W., Melnyk, M., 1990, AJ, 99, 1674

Barsony, M., Chandler, C. J., 1993, ApJ, 406, L71

Beckwith, S. V. W., Sargent, A. I., 1991, ApJ, 381, 250

Beckwith, S. V. W., Sargent, A. I., Chini, R. S., Güsten, R., 1990, AJ, 99, 924

Beichman, C. A., Myers, P. C., Emerson, J. P., Harris, S., Mathieu, R., Benson, P. J., Jennings, R. E., 1986, ApJ, 307, 337

Bieging, J. H., Cohen, M., Schwartz, P. R., 1984, ApJ, 282, 699

Brown, D. W., Chandler, C. J., 1998, MNRAS, submitted

Butner, H. M., Evans, N. J., Harvey, P. M., Mundy, L. G., Natta, A., Randich, M. S., 1990, ApJ, 364, 164

Cabrit, S., André, P., 1991, ApJ, 379, L25

Chandler, C. J., Sargent, A. I., 1993, ApJ, 414, L29

Chandler, C. J., Koerner, D. W., Sargent, A. I., Wood, D. O. S., 1995, ApJ, 449, L139

Chandler, C. J., Terebey, S., Barsony, M., Moore, T. J. T., Gautier, T. N., 1996, ApJ, 471, 308

Chen, H., Myers, P. C., Ladd, E. F., Wood, D. O. S., 1995, ApJ, 445, 377

Ciolek, G. E., Mouschovias, T. C., 1994, ApJ, 425, 142

Clark, F. O., 1991, ApJS, 75, 611

Cohen, M., Fuller, G. A., 1985, ApJ, 296, 620

Cohen, M., Harvey, P. M., Schwartz, R. D., Wilking, B. A., 1984, ApJ, 278, 671

Duncan, W. D., Robson, E. I., Ade, P. A. R., Griffin, M. J., Sandell, G., 1990, MNRAS, 243, 126

Edwards, S., Snell, R. L., 1984, ApJ, 281, 237

Elias, J. H., 1978, ApJ, 224, 857

Foster, P. N., Chevalier, R. A., 1993, ApJ, 416, 303

Herbst, R. M., Koresko, C. D., Leinert, C., 1995, ApJ, 444, L93

Hobson, M. P., Padman, R., 1994, MNRAS, 266, 752

Hogerheijde, M. R., van Dishoeck, E. F., Blake, G. A., van Langevelde, H. J., 1997, ApJ, 489, 293

Hogerheijde, M. R., van Dishoeck, E. F., Blake, G. A., van Langevelde, H. J., 1998, ApJ, in press

Kenyon, S. J., Calvet, N., Hartmann, L., 1993, ApJ, 414, 676 (KCH)

Kenyon, S. J., Gomez, M., Marzke, R. O., Hartmann, L., 1994a, AJ, 108, 251

Kenyon, S. J., Dobrzycka, D., Hartmann, L., 1994b, AJ, 108, 1872

Koerner, D. W., Chandler, C. J., Sargent, A. I., 1995, ApJ, 452, L69

Ladd, E. F., Adams, F. C., Casey, S., Davidson, J. A., Fuller, G. A., Harper, D. A., Myers, P. C., Padman, R., 1991, ApJ, 382, 555

Lay, O. P., Carlstrom, J. E., Hills, R. E., Phillips, T. G., 1994, ApJ, 434, L75

Leinert, C., Haas, M., 1989, ApJ, 342, L39

Lizano, S., Shu, F. H., 1989, ApJ, 342, 834

Mangum, J. G., 1993, PASP, 105, 117

Mannings, V., Emerson, J. P., 1994, MNRAS, 267, 361

Moriarty-Schieven, G. H., Wannier, P. G., Keene, J., Tamura, M., 1994, ApJ, 436, 800

Myers, P. C., Fuller, G. A., Mathieu, R. D., Beichman, C. A., Benson, P. J., Schild, R. E., Emerson, J. P., 1987, ApJ, 319, 340

Neugebauer, G., et al. 1988, in Beichman, C. A., Neugebauer, G., Habing, H. J., Clegg, P. E., & Chester, T. J., eds, IRAS Explanatory Supplement, NASA RP-1190, Washington D. C., p. VI-1

Ohashi, N., Hayashi, M., Ho, P. T. P., Momose, M., Tamura, M., Hirano, N., Sargent, A. I., 1997, ApJ, 488, 317

Osterloh, M., Beckwith, S. V. W., 1995, ApJ, 439, 288

Preibisch, T., Sonnhalter, C., Yorke, H. W., 1995, A&A, 299, 144

Press, W. H., Flannery, B. P., Teukolsky, S. A., Vetterling, W. T., 1986, "Numerical Recipes: The Art of Scientific Computing," Cambridge University Press, Cambridge

Reipurth, B., Chini, R., Krügel, E., Kreysa, E., Sievers, A., 1993, A&A, 273, 221

Saraceno, P., André, P., Ceccarelli, C., Griffin, M., Molinari, S., 1996, A&A, 309, 827

Scoville, N. Z., Kwan, J., 1976, ApJ, 206, 718

Shu, F. H., 1977, ApJ, 214, 488

Shu, F. H., Adams, F. C., Lizano, S., 1987, ARA&A, 25, 23

Strom, K. M., Strom, S. W., Wolff, S. C., Morgan, J., Wenz, M., 1986, ApJS, 62, 39

Terebey, S., Shu, F. H., Cassen, P. C., 1984, ApJ, 286, 529 (TSC)

Terebey, S., Vogel, S. N., Myers, P. C., 1989, ApJ, 340, 472

Terebey, S., Chandler, C. J., André, P., 1993, ApJ, 414, 759

Ward-Thompson, D., Scott, P. F., Hills, R. E., André, P., 1994, MNRAS, 268, 276

Weaver, W. B., Jones, G., 1992, ApJS, 78, 239

Wolfire, M. G., Churchwell, E., 1994, ApJ, 427, 889

This preprint was prepared with the AAS LaTeX macros v4.0.

Table 1. Summary of millimetre/submillimetre observations.

Source	IRAS name	R.A. (1950) (h m s)	Dec. (1950) (° ′ ″)	observing date	type of observation
Haro 6-10	04263+2426	04 26 22.0	+24 26 30	9/91	790 μm map, photometry
TMC1A	04365+2535	04 36 31.2	+25 35 56	9/90	1.1 mm, 790 μm maps
				9/91	photometry
TMC1	04381+2540	04 38 08.5	+25 40 53	9/91	790 μm map, photometry

Table 2. Results of mm/submm photometry, and colour-corrected IRAS flux densities.

λ (mm)	θ_{beam} (arcsec)	F_ν (Jy)[a] Haro 6-10	TMC1A	TMC1
1.927	28	< 0.16	< 0.27	< 0.29
1.260	21	0.099±0.030	0.296±0.032	0.136±0.034
1.104	19	0.179±0.017	0.355±0.012	0.099±0.015
	integrated[b]	···	0.544±0.061	···
0.790	16	0.571±0.044	1.072±0.082	0.300±0.018
	integrated[b]	0.621±0.092	1.59±0.17	0.598±0.083
0.443	19	2.37±0.50	2.77±0.67	2.79±0.52
0.100	···	47±11	46.0±8.3	16.3±2.4
0.060	···	58.4±9.7	34.9±4.8	10.4±1.1
0.025	···	37.6±3.2	7.80±0.72	2.32±0.25
0.012	···	16.6±2.2	1.44±0.19	0.530±0.079

[a]The errors for the mm/submm points are statistical only. The estimated uncertainties in the absolute flux density scale due to the calibration at 2 mm, 1.3 mm, 1.1 mm, 790 μm, and 450 μm are 20, 15, 10, 15, and 30 per cent respectively, and are included in the spectral energy distributions of Fig. 4. The errors on the IRAS flux densities include both statistical and calibration uncertainties, as described in the text. Upper limits are 3 σ.

[b]Flux density integrated over a 5×5-pixel^2 box centered at the peak of the emission in each map.

Table 3. Best-fit parameters for our envelope model.

Source	$L_{\rm bol}$[a] ($L_\odot$)	$M_{\rm env}$ ($M_\odot$)	r_0 (AU)	T_{100}[b] (K)	$T_{\rm range}$[c] (K)	$\langle T \rangle$[d] (K)	p	β
TMC1	0.62	0.031±0.022	13±11	61±18	33−54	22	0.93±0.25	1.33±0.31
TMC1A	1.90	0.027±0.031	16±22	76±38	41−66	28	0.81±0.30	1.46±0.59
Haro 6-10	6.98	0.016±0.013	3.6±3.3	84±32	51−84	32	1.22±0.11	1.41±0.36

[a]Total source luminosity derived from the spectra in Fig. 4.

[b]Value of T at $r = 100$ AU.

[c]Range in values of T_{100} which are consistent with the radiative transfer models of Butner et al. (1990), Wolfire & Churchwell (1994), and Preibisch et al. (1995).

[d]Mass-weighted mean temperature for the best-fit envelope model.

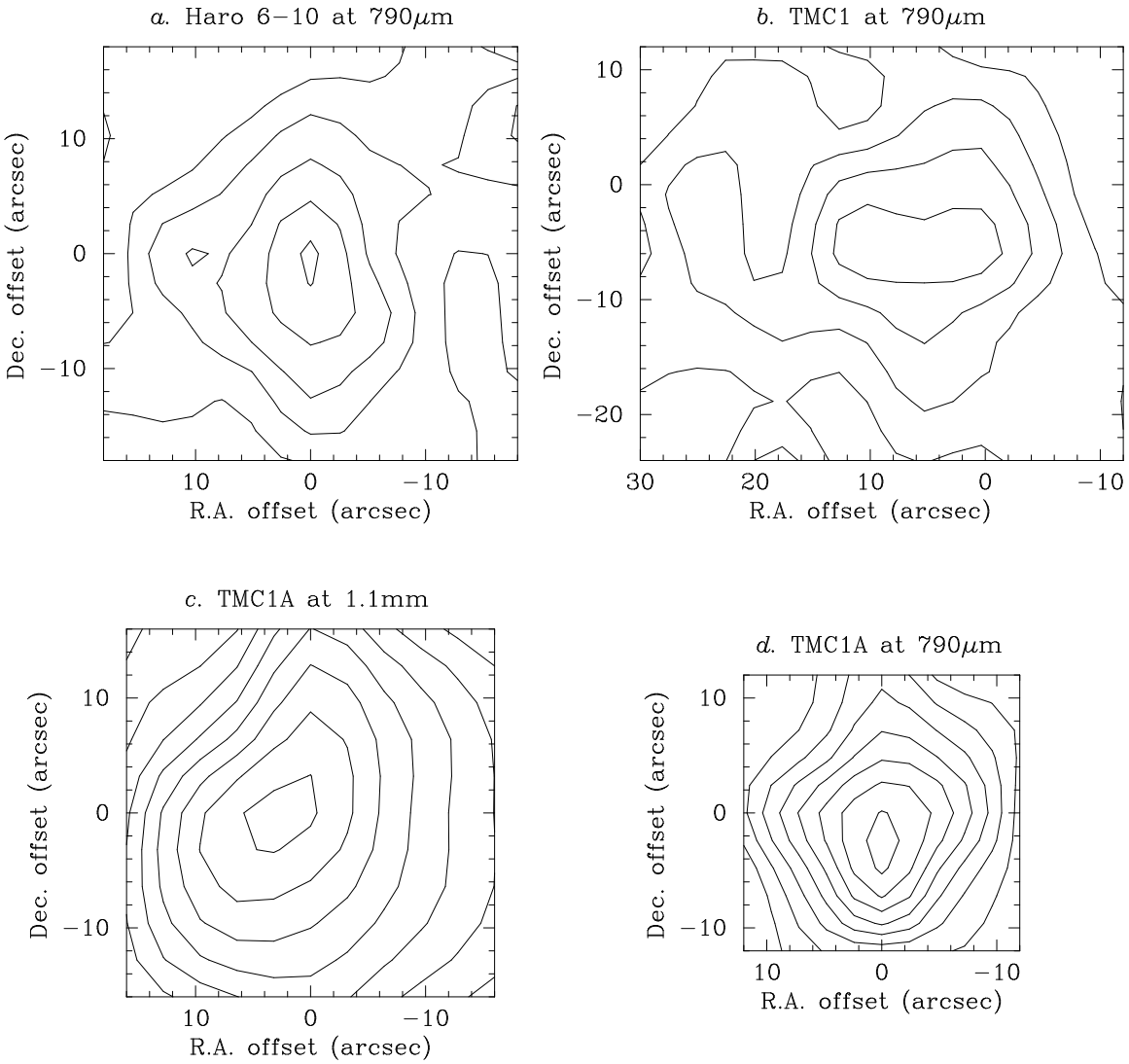

Fig. 1.— Continuum maps of (*a*) Haro 6-10 at λ 790 μm, (*b*) TMC1 at λ 790 μm, (*c*) TMC1A at λ 1.1 mm, and (*c*) TMC1A at λ 790 μm. Contours are spaced at 1.5 σ intervals of 66, 60, 47 and 125 mJy beam^{-1} respectively.

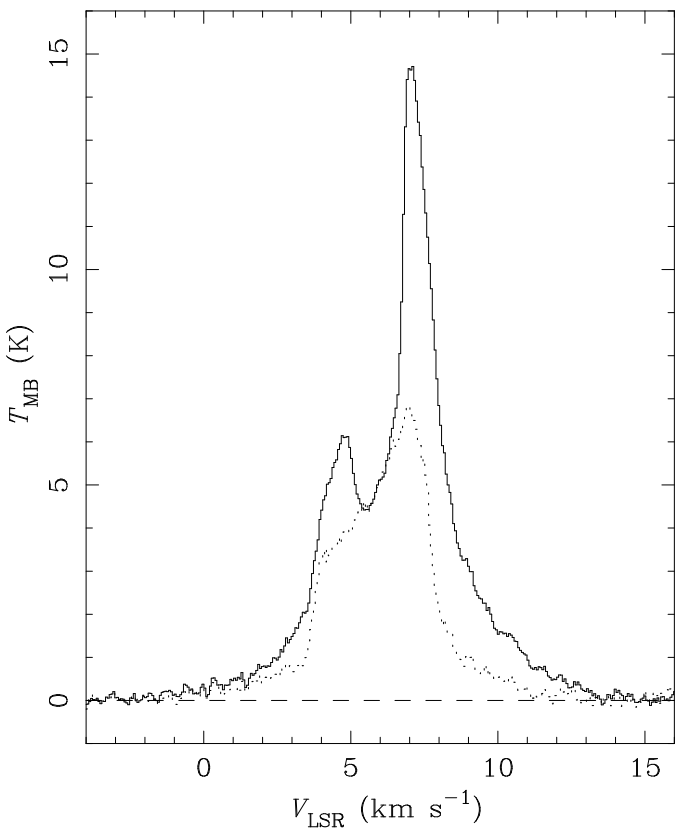

Fig. 2.— CO(2–1) spectra of Haro 6-10. Solid line: a spectrum centred on Haro 6-10; dotted line: the emission averaged over the full 2×2-arcmin^2 area mapped. Non-Gaussian wing emission is clearly present in both spectra, and in the average line profile the optically-thin, blueshifted component first identified by Edwards & Snell (1984) is also evident. The systemic $V_{\rm LSR}$ is 6.5 km s^{-1}.

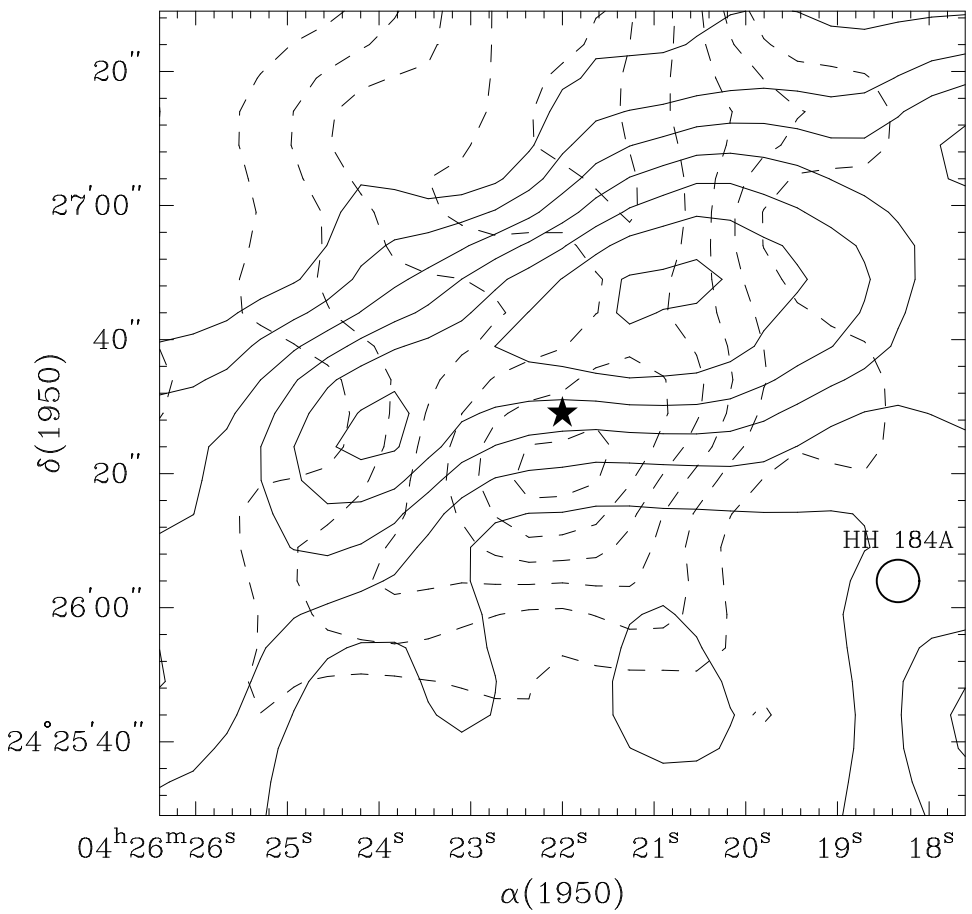

Fig. 3.— The blueshifted (solid contours) and redshifted (dashed contours) CO(2–1) emission from Haro 6-10. A star marks the location of the protostellar binary system, and a circle the Herbig Haro object HH 184A. The CO(2–1) emission is integrated between $|V - V_{\rm LSR}|$ = 3 and 6 km s^{-1}, and the contours are spaced at 0.6, 1.2, 1.8, 2.4,... K km s^{-1}. The rms noise is 0.16 K km s^{-1}.

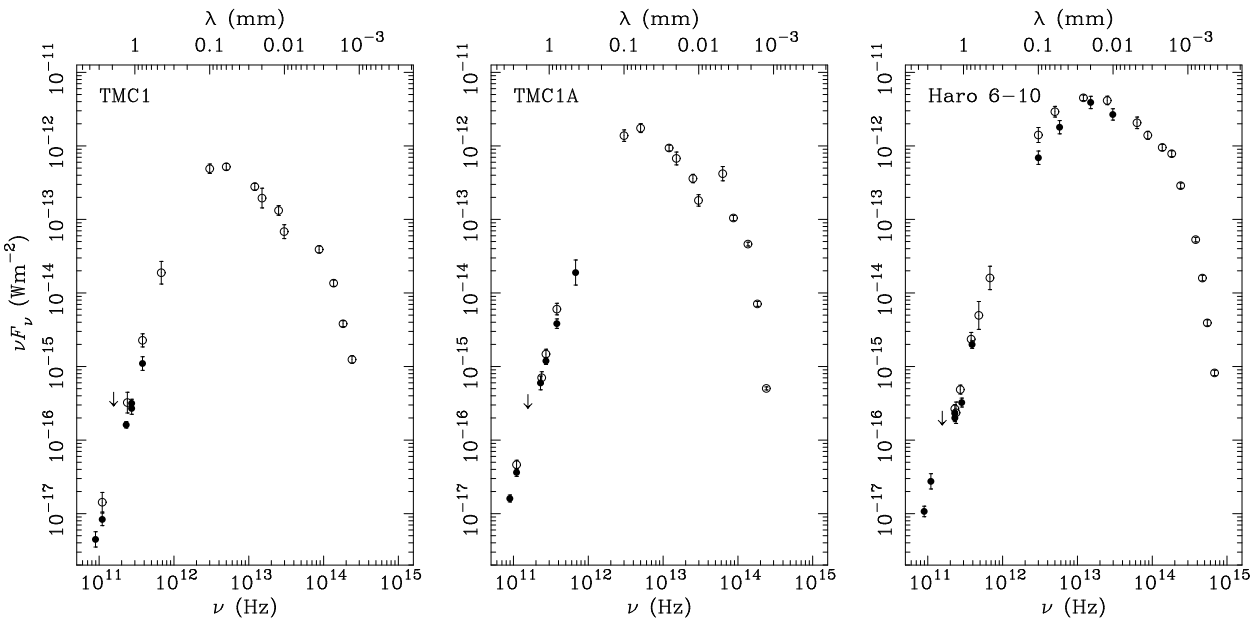

Fig. 4.— Spectral energy distributions of TMC1, TMC1A, and Haro 6-10. Flux densities have been compiled from the literature: IRAS measurements – Point Source Catalog; Kenyon et al. 1994a; Clark 1991; Beichman et al. 1986; Weaver & Jones 1992; this paper. Far-infrared photometry – Cohen et al. 1984. Optical/near-infrared photometry – Myers et al. 1987. Millimetre/submillimetre measurements – Terebey, Chandler, & André 1993; Saraceno et al. 1996; Moriarty-Schieven et al. 1994; Reipurth et al. 1993; Cabrit & André 1991; Osterloh & Beckwith 1995; Beckwith & Sargent 1991; Hogerheijde et al. 1997; Brown & Chandler 1998. Integrated flux densities or measurements obtained with large beams are denoted by open circles, while measurements obtained in single beams which may have missed extended emission are given by filled circles.

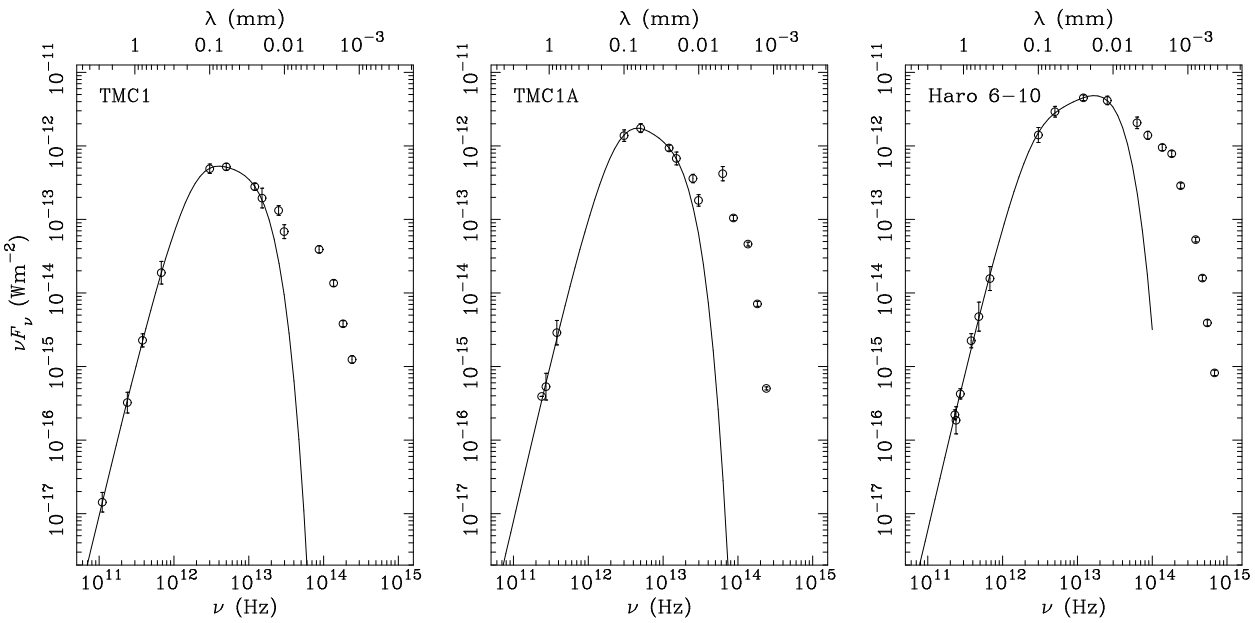

Fig. 5.— Envelope SEDs for TMC1, TMC1A, and Haro 6-10, plotted together with the best-fit envelope models summarized in Table 3.